Actively-monitored periodic-poling in thin-film lithium niobate photonic waveguides with ultrahigh nonlinear conversion efficiency of 4600 %W^{-1}cm^{-2}

ASHUTOSH RAO,[1,3,4] KAMAL ABDELSALAM,[1,4] TRACY SJAARDEMA,[1] AMIRMAHDI HONARDOOST,[1,2] (iD) GUILLERMO F. CAMACHO-GONZALEZ,[1] AND SASAN FATHPOUR[1,2,*] (iD)

[1] *CREOL, The College of Optics and Photonics, University of Central Florida, Orlando, Florida 32816, USA*
[2] *Department of Electrical and Computer Engineering, University of Central Florida, Orlando, Florida 32816, USA*
[3] *Currently with the Physical Measurement Laboratory, National Institute of Standards and Technology, Gaithersburg, Maryland 20899, USA, and the University of Maryland, College Park, Maryland 20742, USA*
[4] *These authors contributed equally*
[*] *fathpour@creol.ucf.edu*

Abstract: Chip-scale implementations of second-order nonlinear optics benefit from increased optical confinement that can lead to nonlinear interaction strengths that are orders of magnitude higher than bulk free-space configurations. Here, we present thin-film-based ultraefficient periodically-poled lithium niobate nonlinear waveguides, leveraging actively-monitored ferroelectric domain reversal engineering and nanophotonic confinement. The devices exhibit up to 4600 %W^{-1}cm^{-2} conversion efficiency for second-harmonic generation, pumped around 1540 nm. In addition, we measure broadband sum-frequency generation across multiple telecom bands, from 1460 to 1620 nm. As an immediate application of the devices, we use pulses of picojoule-level energy to demonstrate second-harmonic generation with over 10% conversion in a 0.6-mm-long waveguide. Our ultracompact and highly efficient devices address growing demands in integrated-photonic frequency conversion, frequency metrology, atomic physics, and quantum optics, while offering a coherent link between the telecom and visible bands.

1. Introduction

Integrated nonlinear optical sources and amplifiers of coherent light [1–20] are key components towards the miniaturization of many different optical systems [21–25]. In contrast to early nonlinear optical frequency converters, modern chip-scale nonlinear devices can provide much higher frequency conversion efficiency. This is facilitated by the nanophotonic confinement inherent to such integrated approaches. Furthermore, they offer the potential to realize sophisticated and unconventional interactions, driven by the enhanced and nanometer-scale precision patterning offered by advanced semiconductor lithography that permits meticulous and scalable device engineering. Many of the applications of such integrated devices are currently the subject of intense study, including second- [1–15], third- [12,16], and high-harmonic generations [26], spectral translation [17], frequency combs and dual-comb spectroscopy [18–22], optical frequency synthesizers and atomic clocks [23–25], telecommunications [27,28], quantum-correlated and entangled photon-state generation [29–34] and quantum-frequency conversion [35–37].

In particular, second-order nonlinear photonics, based on the second-order nonlinearity ($\chi^{(2)}$) of noncentrosymmetric materials, is key to many of the above applications. A few integrated platforms are being pursued for $\chi^{(2)}$-based photonics. To this end, some common nonlinear

materials being used include lithium niobate (LN) [2–8], aluminum nitride [9,10], compound semiconductors [11], and silicon nitride [12–15]. Among them, LN has been the traditional workhorse of nonlinear and quantum optics, offering high optical nonlinear coefficients and broadband optical transmission. Periodically-poled LN (PPLN) crystals and diffused waveguides, where the ferroelectric domains of LN are periodically reversed for quasi-phase matching (QPM), have been widely utilized [38–42]. While the diffused waveguides avoid the interaction bandwidth limitations imposed by high finesse cavities commonly employed in chip-scale nonlinear photonics [6–10], their nonlinear conversion efficiencies have been limited by the nonlinear overlaps as a result of the large sizes of the interacting modes [38,43].

In the past decade, there has been a significant effort towards realizing thin-film lithium niobate (LN) photonic devices, motivated by the promise of the vastly increased electrooptic (EO) and nonlinear optical interaction strengths driven by tightly confined optical modes [43,44]. Impressive progress has been made with demonstrations of microresonators [6–8], EO modulators [45], $\chi^{(2)}$-based nonlinear frequency converters [2–8], photonic crystals [46], frequency combs [47], and electric-field and temperature sensors [48,49]. The low-loss waveguiding platforms [50] are capable of also supporting important passive elements such as Bragg [51] and arrayed-waveguide gratings [52]. Coupling elements, such as grating couplers, have been integrated with EO modulators as well [53–56].

In this Article, we improve on the state-of-the-art nonlinear conversion efficiency of diffused PPLN waveguides by over an order of magnitude with periodically-poled nanowaveguides that show up to $4600\,\%\mathrm{W}^{-1}\mathrm{cm}^{-2}$ efficiency for second-harmonic generation (SHG) using telecom-band pump light. We optimize the ferroelectric domain inversion by monitoring the nonlinear conversion efficiency of our waveguides in an iterative, reversible and actively-monitored poling process. We then use our optimized devices to demonstrate sum-frequency generation (SFG) with pump wavelengths spanning across a broad operating range from 1460 nm to 1620 nm. Finally, we leverage the broad and continuous conversion bandwidth of the waveguide via pulsed pumping with picojoule-level energy pulses to show SHG in a 0.6-mm-long waveguide that saturates around 1 mW of average pump power.

2. Nano-PPLN design and fabrication

The essential conditions for efficient nonlinear optical processes are energy conservation, momentum conservation, high nonlinear coefficients, and strong nonlinear overlap. The second-harmonic (sum-frequency) process involves one (two) pump mode(s) in the telecom bands and one nonlinear signal at visible wavelengths. Energy conservation imposes the condition $\omega_1 + \omega_2 = \omega_3$ and momentum conservation implies zero momentum mismatch, i.e., $\Delta\beta = \beta_1 + \beta_2 - \beta_3 - 2\pi m/\Lambda = 0$, where ω_1 and ω_2 and β_1 and β_2 are the telecom pump frequencies and propagation constants, and ω_3 and β_3 are the frequency and propagation constant of the generated visible light. Λ is the poling period for QPM, where periodic ferroelectric domain reversal is used to compensate for the mismatch of the wavevectors of the interacting optical fields, and m is the order of QPM ($m = \pm 1, \pm 3$, etc.). ω_3 is constrained by our choice of ω_1 and ω_2 in the telecom bands, and $\beta_i = n_{\mathrm{eff},i}\omega_i/c$ are dictated by the frequencies and the effective indices ($n_{\mathrm{eff},i}$) of their corresponding optical modes in the waveguide, where c is the speed of light in vacuum. For SHG, $\omega_1 = \omega_2 = \omega_3/2$ and $\beta_1 = \beta_2$. The small-signal SHG response is $P_{2\omega} = \eta P_\omega^2 L^2$ [57], where $P_{2\omega}$ is the power generated at the second harmonic (SH) in the device, P_ω is the pump power input at the fundamental wavelength, and L is the length of the nonlinear waveguide. η is the normalized nonlinear conversion efficiency, given by $\eta = 16\omega^2(\kappa_{\mathrm{SHG}}^{(2\omega)})^2\mathrm{sinc}^2(\Delta\beta(\omega)L/2)$, where $\kappa_{\mathrm{SHG}}^{(2\omega)} = \varepsilon_0 \int_{-\infty}^{\infty}\int_{-\infty}^{\infty} d_{33}\tilde{e}_1^2\tilde{e}_2^*\,dxdy$ is the SHG coupling efficiency, $e_1(x,y)$ and $e_2(x,y)$ are the field distributions of the guided eigenmodes at ω and 2ω, respectively, and d_{33} is the largest nonlinear coefficient of LN [57]. It can be shown that $\kappa_{\mathrm{SHG}}^{(2\omega)} \propto 1/\sqrt{A_{\mathrm{eff}}}$, where A_{eff} is the nonlinear

interaction area, calculated as

$$A_{\text{eff}} = \frac{\left[\left\{\iint |E_{2\omega}(x,y)|^2 dxdy\right\}\left\{\iint |E_{\omega}(x,y)|^2 dxdy\right\}^2\right]}{\left[\left\{\iint \bar{\chi}^{(2)}(x,y)E_{\omega}^2(x,y)E_{2\omega}(x,y)dxdy\right\}^2\right]},$$

where $\bar{\chi}^{(2)}(x,y)$ is the normalized second-order nonlinear coefficient.

Our choice of a nanoscale waveguide, supported by the thickness and crystal orientation of a thin film of LN (300 nm and *X*-cut) along with the strong refractive index contrast of the LN waveguide core to the upper air and lower silicon dioxide (SiO$_2$) cladding layer, is key to realizing high nonlinear conversion efficiency through smaller A_{eff}. Figure 1(a) shows the scaling of the nonlinear conversion efficiency with A_{eff}, clearly indicating the potential of using nanophotonic confinement to realize enhanced nonlinear efficiency in devices such as those in this work. Optical and scanning-electron micrographs are included in Fig. 1(b), and a schematic is shown in Fig. 1(c). The electric-field distribution of the fundamental transverse-electric (TE) pump and second-harmonic (SH) modes used here for a ridge width and etch depth of 1.5 μm and 100 nm are plotted in Fig. 1(d). We choose the poling period for QPM between the fundamental
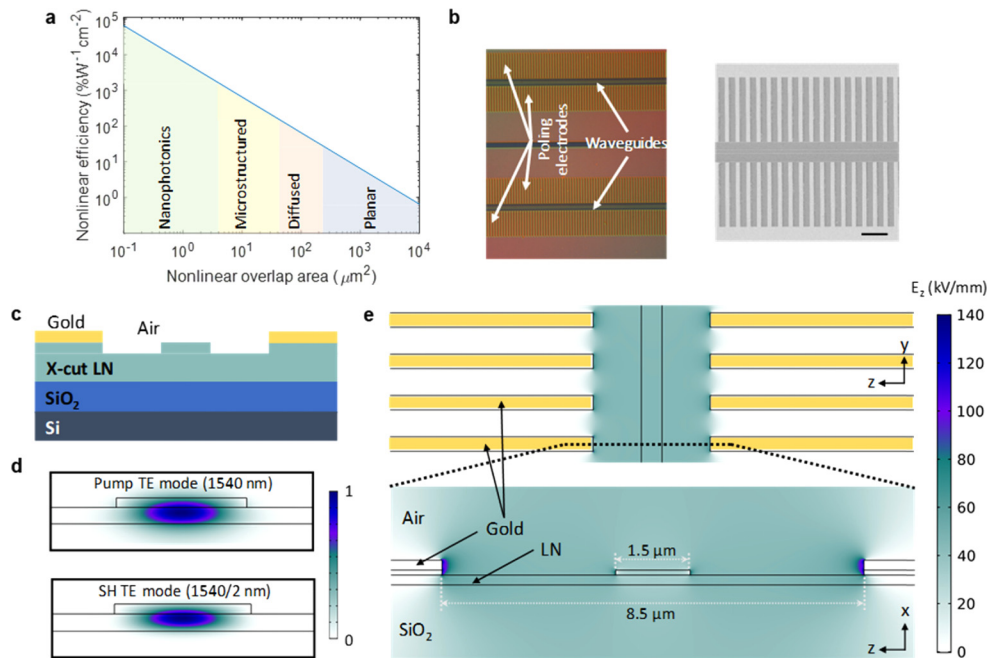

Fig. 1. Nonlinear efficiency and nanophotonic periodically-poled lithium niobate waveguide. (a) Comparison of normalized nonlinear conversion efficiency between various collinear geometries. The nonlinear overlap area is an effective interaction area for a given pair of modes that reduces with increasing optical confinement. Nanophotonic waveguides can offer high conversion efficiencies because of their small optical modes and strong nonlinear interaction. (b) Optical and scanning-electron micrographs of a nanophotonic periodically-poled lithium niobate nonlinear waveguide. (c) Schematic showing ridge waveguide and poling electrodes on a *X*-cut thin film of lithium niobate on an oxidized silicon substrate. (d) Electric field distributions of the fundamental transverse-electric modes at pump and second harmonic wavelengths of 1540 nm and 770 nm. (e) Cross-sections in the *y-z* and *x-z* planes extracted from 3-D finite-element method simulations of the electric poling field with an applied poling voltage of 400 V, as used experimentally in this work.

pump and modes, maximizing the nonlinear interaction strength. Using higher order modes would increase A_{eff} and degrade the nonlinear overlap. Our choice of Y-propagating TE modes is concomitant with the X-cut crystal orientation of the LN thin-film, permitting the use of the highest nonlinear tensor coefficient of LN, d_{33}, as well as periodic inversion of the ferroelectric domains, which are parallel to the crystal Z-axis. We choose $\Lambda = 2.67$ µm to effect first-order QPM, i.e., $m = \pm 1$. Cross-sections extracted from a 3-D electrostatic finite-element method simulation used to study the distribution of the electric poling field are shown in Fig. 1(e). The thin film mitigates the difficulty of realizing poling periods that are much shorter than those required in diffused PPLN waveguides.

The device fabrication begins with wafer-scale fabrication of the thin-film LN substrates [43]. Helium ion implantation on bulk single-crystal X-cut LN wafers is the first step. The implantation energy is calculated using a Monte-Carlo simulator. The implanted wafers are then bonded at the implanted surface at room temperature in a vacuum chamber to a layer of silicon dioxide grown on a standard silicon wafer. The LN-Si wafer combination is then heated to thermally exfoliate the implanted LN layer onto the SiO_2 layer. The Si wafer with the thin-film of LN is annealed to recover the desired nonlinear coefficients of LN, and finally undergoes chemical-mechanical polishing. Nonlinear waveguides are then fabricated on thin-film LN dies with 300 nm thick LN device layer. We use standard lithography to define metal alignment markers and poling electrodes, and waveguides. The metal layers are formed by a lift-off of a chrome-gold layer (5 nm and 150 nm thick respectively) in a common organic solvent, N-Methyl-2-pyrrolidone, heated to 120°C, and the waveguides are patterned by dry etching in an argon plasma. The waveguide facets are then diced and polished. Oxygen plasma is used multiple times throughout the fabrication for de-scum and cleaning steps.

3. Actively-monitored second harmonic generation

We monitor the SHG power in-situ during the periodic poling process and use it as feedback to optimize the periodic poling parameters. The high voltage pulses used for periodic poling are generated by an arbitrary-waveform generator (AWG), monitored using a digital oscilloscope (OSC), and then amplified by a high voltage amplifier (HVA). The pulses are passed to the poling electrodes on the chip using standard tungsten contact probes to generate strong electric fields across the waveguide region higher than the coercive field for poling LN (21 kV/mm). Depoling can be carried out by applying a series of periodic pulses with inverse polarity and the waveguide can be subsequently repoled. To characterize SHG, pump light from a commercial tunable telecom continuous-wave (CW) laser is directly coupled into the waveguide at the polished chip facet using a lensed fiber. A polarization controller (PC) is used to control the polarization of the pump light. The nonlinear signal is generated on the chip, out-coupled along with the residual pump using another lensed fiber and measured using calibrated photodetectors (PDs) in the telecom and visible bands. The experimental setup is shown in Fig. 2(a). Such a setup permits repeated quantitative investigation of the optimal poling for a waveguide, thereby offering a unique complement to typical physical end-of-poling characterization, such as wet etching [58], piezo-force microscopy [59,60] and micro-Raman measurements [61].

The parameter space for periodic poling includes the voltage (or electric field), pulse duration, and repetition period, among other factors. After an initial exploration, we settle on 400 V and 5 ms duration pulses with a 5 second repetition period. This pulse duration is shorter than the ∼ 100 ms pulses required to pole bulk and diffused waveguide PPLN [62] and can be attributed to the smaller poling period required in this work. The average poling electric field is ∼ 40 kV/mm, and no dielectric breakdown of air is observed. We use an optically-monitored iterative poling, depoling, and repoling sequence. The depoling step is continued after the SH power drops below the picowatt noise floor of the detector. The repetition of such a poling sequence may assist domain nucleation. We first periodically pole a 0.6-mm-long nano-PPLN waveguide and record
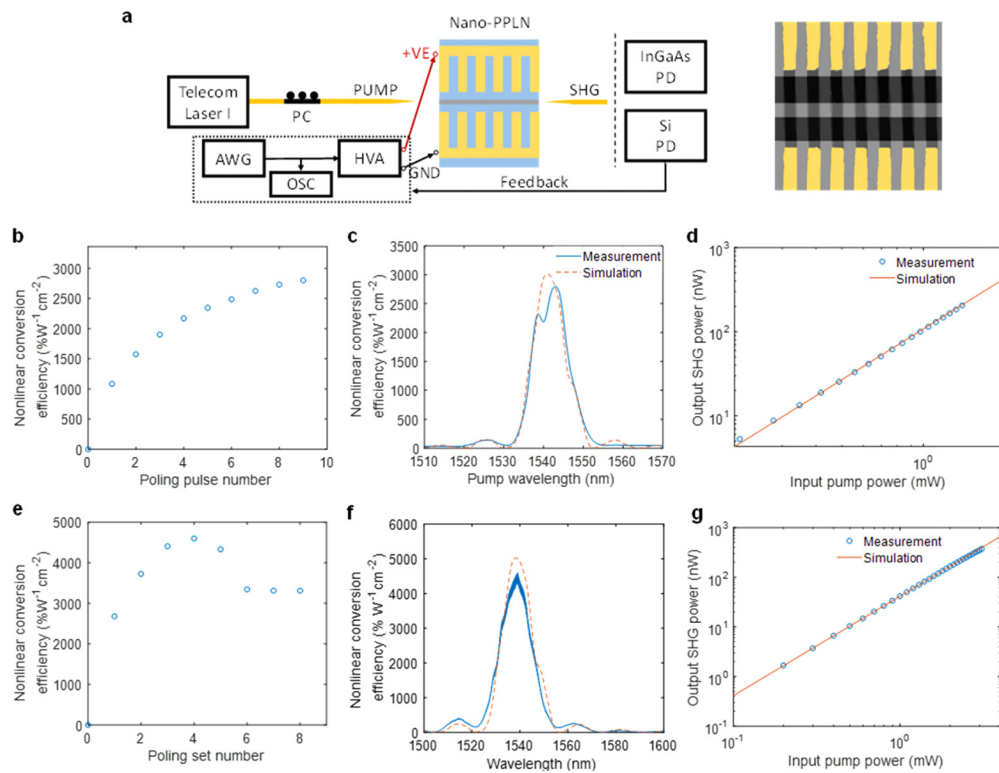
Fig. 2. Second-harmonic generation and poling. (a) Experimental setup for optimizing the periodic poling in-situ by measuring the second harmonic power during poling, and false color atomic force micrograph showing regular periodic poling using across the waveguide after wet etching (electrode duty cycle ~ 0.5). AWG: arbitrary waveform generator, OSC: digital oscilloscope, HVA: high voltage amplifier, PC: polarization controller, PD: calibrated photodetector. (b-d) First device: (b) Increase of SHG efficiency with the number of poling pulses used for ferroelectric domain inversion. (c) Measured peak conversion efficiency of $2800\%W^{-1}cm^{-2}$. (d) Quadratic power dependence of SHG on pump power. (e-g) Second device: (e) Increase of SHG efficiency with the number of poling cycles used for ferroelectric domain inversion. The efficiency reaches a maximum and then decreases before saturating; (f) Measured peak conversion efficiency of $4600\,\%W^{-1}cm^{-2}$. (g) Quadratic scaling of SHG power with pump power.

the peak SHG efficiency with increasing electrical poling pulse numbers, as shown in Fig. 2(b). After 9 poling pulses, we measure a peak normalized conversion efficiency of $2800\%\,W^{-1}cm^{-2}$ at 1540 nm (Fig. 2(c)). The conversion efficiency is calculated after accounting for asymmetric waveguide coupling losses at the two wavelengths. The individual coupling losses (6 and 7 dB per facet for pump and SHG, respectively) are measured separately prior to optimizing the input and output for pump and SH coupling for the SHG experiment. The complete lack of any SH signal prior to poling confirms the absence of any unintentional or accidentally phase-matched nonlinear processes, in keeping with our simulations (Fig. 2(c)). These simulations include a correction factor to account for the mismatch between the measured and theoretical peak efficiencies ($2800\%\,W^{-1}cm^{-2}$ and $5500\%\,W^{-1}cm^{-2}$ (Fig. 1(a)). The propagation losses are 3 and 7 dB/cm at pump and SHG, respectively, as measured by Fabry Perot fringes. The effect of propagation loss is numerically confirmed to be small; this is due to the sub-millimeter length of our device. The poling duty cycle is between 45% and 50%, as seen in Fig. 2(a) by atomic force

microscopy. The quadratic scaling of the SHG (Fig, 2(d)) shows good agreement with simulations after correction. We reserve this first device for further sum-frequency and cascaded harmonic generation experiments, presented later. We calculate an uncertainty of $\pm 250\%$ W^{-1}cm^{-2} in the conversion efficiency, arising from the measured uncertainty of the absolute transmission at the two wavelengths.

Next, we pick a different waveguide to investigate the theoretical efficiency limit. This device is a 0.3-mm-long nano-PPLN waveguide with a similar cross-section and different poling period. After repeating our initial poling procedure, we measure a peak normalized conversion efficiency of 2800% W^{-1}cm^{-2} (Fig. 2(e)), thereby confirming the repeatability of our initial poling process. This is followed by a series of depoling and repoling cycles, where the specifics are as described earlier with poling pulse length increasing monotonically from 15 to 30 ms to achieve higher SHG efficiency. This process continues until the saturation of the SHG power. The transition through a maximum to the overpoling regime may imply that both poling uniformity and domain nucleation are assisted by the repeated poling. We continue to monitor the peak SHG power at the end of each repoling sequence, as shown in Fig. 2(e). At the end of four such sequences, we measure a record-high conversion efficiency of 4600 % W^{-1}cm^{-2} (Fig. 2(f)), with a calculated uncertainty of $\pm 410\%$ W^{-1}cm^{-2}. The shorter device length may offer an improvement in poling uniformity and efficiency. Continued poling results in an initial decrease followed by saturation of the efficiency. Figure 2(g) confirms the quadratic scaling of the SHG with pump power.

4. Broadband sum frequency generation

SFG can be driven by two widely separated pumps, in contrast to single-pump SHG. The dual-pump interaction offers the ability to generate coherent light in spectral bands where lasers may not be commonly available for SHG. The SFG response is given by $P_{SFG} = \eta_{\mathrm{SFG}} P_{\omega_1} P_{\omega_2} L^2$, which resembles the previously-discussed SHG response. It is the wider bandwidth of $\Delta\beta(\omega_1, \omega_2)$ compared to $\Delta\beta(\omega_1, \omega_1)$ that offers the broader SFG conversion compared to SHG. In our device, the dual-pump SFG interaction offers a significantly increased range of telecom pump wavelengths that can be used for visible-light generation. We measure SFG in our 0.6 mm long device, pumped across the telecom S, C, and L bands (1460 to 1620 nm). Two polarization-controlled telecom lasers are combined using a 50:50 fiber coupler and coupled onto the chip using a lensed fiber (Fig. 3(a)). First, laser II is fixed at 1501 nm and laser I is swept across its tuning range. In Fig. 3(b), SFG between pump laser I and II is observed at 1580 nm, along with SHG of pump laser I around 1540 nm. The different measured amplitudes and bandwidths of the SHG and SFG responses are due to fundamental differences in the efficiencies and phase-matching conditions of the two processes and are reproduced well in simulation (see Figs. 3(d) and 3(e)). Figure 3(c) shows the expected linear power-scaling of the SFG signal.

Next, we measure the full two-wavelength SFG response of the device by sweeping both laser wavelengths iteratively. Such a characterization of the SFG QPM expands on typical SFG experiments, where the wavelength of one of the pump lasers is kept fixed. The two-wavelength response is shown in Fig. 3(d) with a clear SFG signal, represented by the main diagonal in the sampled wavelength span. SHG is also present whenever the wavelength of the pump lasers overlaps with the SHG bandwidth, resulting in the horizontal and vertical bands at 1540 nm on both axes. The sum of the SHG response and the wideband SFG diagonal leads to the peak when both pumps are around 1540 nm, where the SFG can also be interpreted as two-eigenmode SHG. The slight drop in SFG towards the lower right is due to a decrease in the power of laser II near 1460 nm. Figure 3(d) agrees well with simulations that are presented in Fig. 3(e).
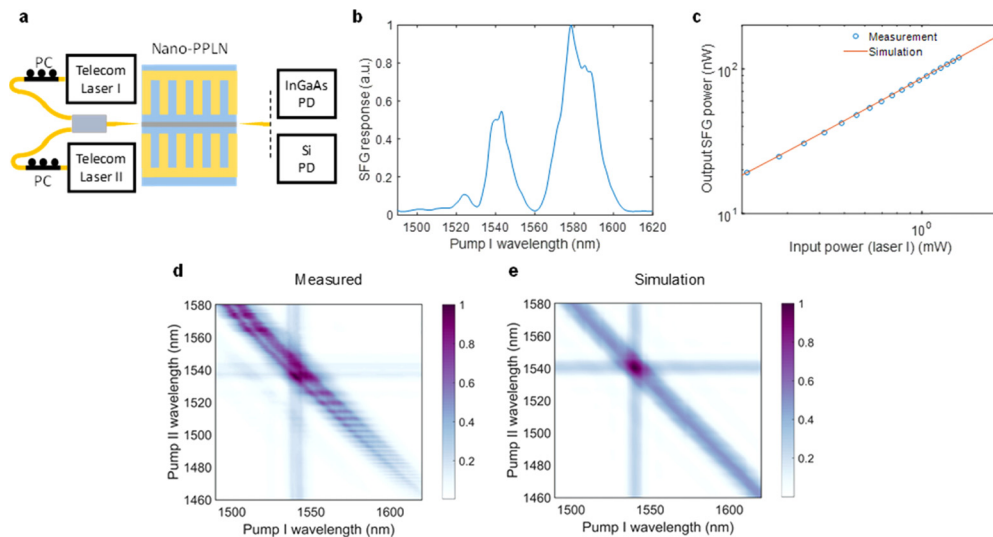
Fig. 3. Broadband sum-frequency generation. (a) Experimental setup; (b) SFG and SHG signals measured around 1580 nm and 1540 nm respectively. Pump laser II is held at 1501 nm. (c) Linear dependence of the SFG on the pump power of laser I. (d) Wideband two-wavelength SFG response measured across 1460 nm to 1620 nm. The wavelength of pump laser I is swept continuously across 1480 nm to 1620 nm, while the wavelength of pump laser II is incremented by 1 nm from 1460 nm to 1580 nm. The main diagonal corresponds to the SFG response. The horizontal and vertical signals, both near 1540 nm, correspond to SHG from the two pump lasers. (e) Simulation of two-wavelength SFG response in good agreement with the measurement in panel (d).

5. Picojoule-level energy pulse pumped second harmonic generation

To demonstrate SHG using low-energy pulses, we use a high numerical aperture lens to couple a collimated beam of polarized pulsed pump light into our first device. A half-wave plate (HWP) and a neutral-density filter (NDF) are used to rotate the polarization and attenuate the pump power as desired. The nonlinear output is collected in a lensed fiber and sent to an optical spectrum analyzer. The pulses are generated in a commercial fiber laser at an 80-MHz repetition rate and 100-fs nominal pulse width. The setup is shown in Fig. 4(a). We observe efficient SHG using pulses centered near 1550 nm wavelength (Figs. 4(b) and (c)). The signature of quadratic scaling is shown in Fig. 4(d), while Fig. 4(e) shows the conversion efficiency in terms of pulse energies. Over 10% conversion is realized for 20 pJ pump pulse energy, where the SHG begins to saturate. This is made possible by a combination of the broad continuous SFG bandwidth and the high optical nonlinearity of our waveguide device, coupled with the high peak power and broad optical spectrum of the employed pulses.

In comparison, most of the spectrum of the pulse would not be resonant with a typical nanophotonic cavity. At the same time, a typical nanophotonic microcavity would offer superior performance for a CW pump, when compared to a compact straight waveguide. It is evident in Figs. 4(b) and (c) that we also observe third- and fourth-harmonic generation (THG and FHG) via cascaded $\chi^{(2)}$ processes – SFG of the pump and SH for THG, and SHG of the SHG of the pump for FHG. High-harmonic generation [26] may be achievable in similar nanophotonic PPLN waveguides via mid-infrared pumping and specific device engineering.
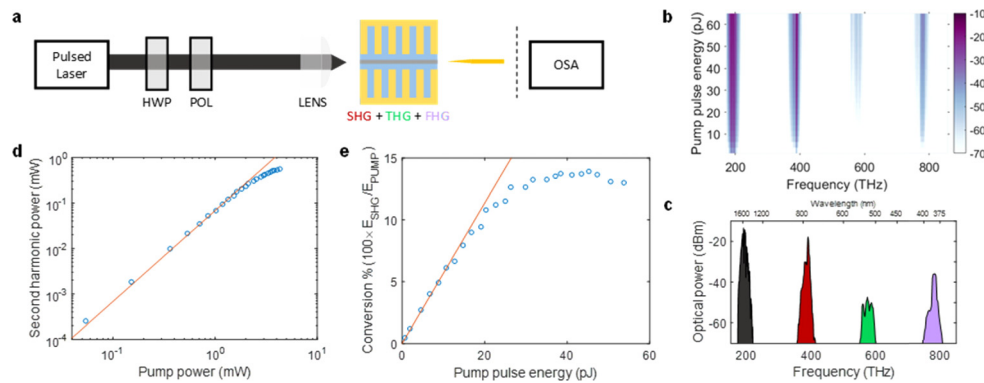
Fig. 4. Low pulse energy second-harmonic generation. (a) Simplified experimental setup. HWP: half-wave plate, NDF: neutral density filter. (b) Nonlinear output spectra in dBm measured over a range of pump pulse energies. (c) Cross-section of panel (b) at maximum pump power. (d) Quadratic average power scaling of pulsed SHG. (e) Pulse energy conversion efficiency in % versus pulse energy of the pump. A conversion efficiency of 10% is obtained with 20 pJ pulses.

6. Summary

In conclusion, our nonlinear LN devices demonstrate efficient second-order nonlinear processes, particularly a record-high SHG conversion efficiency of to $4600\,\%\text{W}^{-1}\text{cm}^{-2}$. The devices leverage modern nanophotonic confinement for enhanced performance, in addition to the well-known high nonlinear optical coefficients and ferroelectric nature of LN. Furthermore, a novel iterative periodic poling procedure that enables in-situ optimization of the ferroelectric domain inversion is developed for the first time. Along with SHG, we show broadband SFG, pumped at wavelengths ranging across 1460 to 1620 nm. By leveraging the broad and continuous nonlinear conversion bandwidth of the waveguides, efficient pulsed SHG that saturates at mW-level average pump power using picojoule-level energy pulses is demonstrated. In conjunction with well-established thin-film LN EO modulators, high-quality factor etalons, and a host of other passive waveguide elements, our results offer the potential to densely integrate efficient EO and nonlinear optical elements on the same thin-film LN chip to realize advanced circuits applicable to telecommunications, frequency metrology, reconfigurable entangled photon-state generation and manipulation, and high harmonic generation and ultrafast optics.

Funding

References

1. J. U. Fürst, D. V. Strekalov, D. Elser, M. Lassen, U. L. Andersen, C. Marquardt, and G. Leuchs, "Naturally phase-matched second-harmonic generation in a whispering-gallery-mode resonator," Phys. Rev. Lett. **104**(15), 153901 (2010).
2. A. Rao, M. Malinowski, A. Honardoost, J. R. Talukder, P. Rabiei, P. Delfyett, and S. Fathpour, "Second-harmonic generation in periodically-poled thin film lithium niobate wafer-bonded on silicon," Opt. Express **24**(26), 29941–29947 (2016).
3. L. Chang, Y. Li, N. Volet, L. Wang, J. Peters, and J. E. Bowers, "Thin film wavelength converters for photonic integrated circuits," Optica **3**(5), 531–535 (2016).
4. A. Rao, J. Chiles, S. Khan, S. Toroghi, M. Malinowski, G. F. Camacho-González, and S. Fathpour, "Second-harmonic generation in single-mode integrated waveguides based on mode-shape modulation," Appl. Phys. Lett. **110**(11), 111109 (2017).

5.   C. Wang, C. Langrock, A. Marandi, M. Jankowski, M. Zhang, B. Desiatov, M. M. Fejer, and M. Lončar, "Ultrahigh-efficiency wavelength conversion in nanophotonic periodically poled lithium niobate waveguides," Optica **5**(11), 1438–1441 (2018).
6.   J. Lin, Y. Xu, J. Ni, M. Wang, Z. Fang, L. Qiao, W. Fang, and Y. Cheng, "Phase-matched second-harmonic generation in an on-chip LiNbO₃ microresonator," Phys. Rev. Appl. **6**(1), 014002 (2016).
7.   R. Wolf, I. Breunig, H. Zappe, and K. Buse, "Cascaded second-order optical nonlinearities in on-chip micro rings," Opt. Express **25**(24), 29927–29933 (2017).
8.   R. Luo, H. Jiang, S. Rogers, H. Liang, Y. He, and Q. Lin, "On-chip second-harmonic generation and broadband parametric down-conversion in a lithium niobate microresonator," Opt. Express **25**(20), 24531–24539 (2017).
9.   X. Guo, C.-L. Zou, and H. X. Tang, "Second-harmonic generation in aluminum nitride microrings with 2500%/W conversion efficiency," Optica **3**(10), 1126–1131 (2016).
10. A. W. Bruch, X. Liu, X. Guo, J. B. Surya, Z. Gong, L. Zhang, J. Wang, J. Yan, and H. X. Tang, "17,000 %/W Second harmonic conversion efficiency in single crystalline aluminum nitride microresonators," arXiv:1807.09638v1 [physics.optics] (2018).
11. D. P. Lake, M. Mitchell, H. Jayakumar, L. F. Dos Santos, D. Curic, and P. E. Barclay, "Efficient telecom to visible wavelength conversion in doubly resonant gallium phosphide microdisks," Appl. Phys. Lett. **108**(3), 031109 (2016).
12. J. S. Levy, M. A. Foster, A. L. Gaeta, and M. Lipson, "Harmonic generation in silicon nitride ring resonators," Opt. Express **19**(12), 11415–11421 (2011).
13. M. W. Puckett, R. Sharma, H.-H. Lin, M. Yang, F. Vallini, and Y. Fainman, "Observation of second-harmonic generation in silicon nitride waveguides through bulk nonlinearities," Opt. Express **24**(15), 16923–16933 (2016).
14. A. Billat, D. Grassani, M. H. P. Pfeiffer, S. Kharitonov, T. J. Kippenberg, and C.-S. Brés, "Large second harmonic generation enhancement in Si₃N₄ waveguides by all-optically induced quasi-phase-matching," Nat. Commun. **8**(1), 1016 (2017).
15. D. D. Hickstein, D. R. Carlson, H. Mundoor, J. B. Khurgin, K. Srinivasan, D. Westly, A. Kowligy, I. Smalyukh, S. A. Diddams, and S. B. Papp, "Self-organized nonlinear gratings for ultrafast nanophotonics," arXiv:1806.07547 [physics.optics] (2018).
16. J. B. Surya, X. Guo, C.-L. Zou, and H. X. Tang, "Efficient third-harmonic generation in composite aluminum nitride/silicon nitride microrings," Optica **5**(2), 103–108 (2018).
17. X. Lu, G. Moille, Q. Li, D. A. Westly, A. Singh, A. Rao, S.-P. Yu, T. C. Briles, S. B. Papp, and K. Srinivasan, "Efficient telecom-to-visible spectral translation through ultralow power nonlinear nanophotonics," Nat. Photonics **13**, 593–601 (2019).
18. T. J. Kippenberg, R. Holzwarth, and S. Diddams, "Microresonator-based optical frequency combs," Science **332**(6029), 555–559 (2011).
19. Y. Okawachi, K. Saha, J. S. Levy, Y. H. Wen, M. Lipson, and A. L. Gaeta, "Octave-spanning frequency comb generation in a silicon nitride chip," Opt. Lett. **36**(17), 3398–3400 (2011).
20. H. Jung, C. Xiong, K. Y. Fong, X. Zhang, and H. X. Tang, "Optical frequency comb generation from aluminum nitride microring resonator," Opt. Lett. **38**(15), 2810–2813 (2013).
21. M.-G. Suh, Q. Yang, K. Yang, X. Yi, and K. J. Vahala, "Microresonator soliton dual-comb spectroscopy," Science **354**(6312), 600–603 (2016).
22. A. Dutt, C. Joshi, X. Ji, J. Cardenas, Y. Okawachi, K. Luke, A. L. Gaeta, and M. Lipson, "On-chip dual-comb source for spectroscopy," Sci. Adv. **4**(3), e1701858 (2018).
23. D. T. Spencer, T. Drake, T. C. Briles, J. Stone, L. C. Sinclair, C. Fredrick, Q. Li, D. Westly, B. R. Ilic, A. Bluestone, N. Volet, T. Komljenovic, L. Chang, S. H. Lee, D. Y. Oh, M.-G. Suh, K. Y. Yang, M. H. P. Pfeiffer, T. J. Kippenberg, E. Norberg, L. Theogarajan, K. Vahala, N. R. Newbury, K. Srinivasan, J. E. Bowers, S. A. Diddams, and S. B. Papp, "An optical-frequency synthesizer using integrated photonics," Nature **557**(7703), 81–85 (2018).
24. S. B. Papp, K. Beha, P. Del'Haye, F. Quinlan, H. Lee, K. J. Vahala, and S. A. Diddams, "Microresonator frequency comb optical clock," Optica **1**(1), 10–14 (2014).
25. Z. L. Newman, V. Maurice, T. Drake, J. R. Stone, T. C. Briles, D. T. Spencer, C. Fredrick, Q. Li, D. Westly, B. R. Ilic, B. Shen, M.-G. Suh, K. Y. Yang, C. Johnson, D. M. S. Johnson, L. Hollberg, K. J. Vahala, K. Srinivasan, S. A. Diddams, J. Kitching, S. B. Papp, and M. T. Hummon, "Architecture for the photonic integration of an optical atomic clock," Optica **6**(5), 680–685 (2019).
26. D. D. Hickstein, D. R. Carlson, A. Kowligy, M. Kirchner, S. R. Domingue, N. Nader, H. Timmers, A. Lind, G. G. Ycas, M. M. Murnane, H. C. Kapteyn, S. B. Papp, and S. A. Diddams, "High-harmonic generation in periodically poled waveguides," Optica **4**(12), 1538–1544 (2017).
27. P. Marin-Palomo, J. N. Kemal, M. Karpov, A. Kordts, J. Pfeifle, M. H. P. Pfeiffer, P. Trocha, S. Wolf, V. Brasch, M. H. Anderson, R. Rosenberger, K. Vijayan, W. Freude, T. J. Kippenberg, and C. Koos, "Microresonator-based solitons for massively parallel coherent optical communications," Nature **546**(7657), 274–279 (2017).
28. H. Hu, F. D. Ros, M. Pu, F. Ye, K. Ingerslev, E. P. da Silva, M. Nooruzzaman, Y. Amma, Y. Sasaki, T. Mizuno, Y. Miyamoto, L. Ottaviano, E. Semenova, P. Guan, D. Zibar, M. Galili, K. Yvind, T. Morioka, and L. K. Oxenløwe, "Single-source chip-based frequency comb enabling extreme parallel data transmission," Nat. Photonics **12**(8), 469–473 (2018).

29. J. W. Silverstone, D. Bonneau, K. Ohira, N. Suzuki, H. Yoshida, N. Iizuka, M. Ezaki, C. M. Natarajan, M. G. Tanner, R. H. Hadfield, V. Zwiller, G. D. Marshall, J. G. Rarity, J. L. O'Brien, and M. G. Thompson, "On-chip quantum interference between silicon photon-pair sources," Nat. Photonics **8**(2), 104–108 (2014).

30. D. Grassani, S. Azzini, M. Liscidini, M. Galli, M. J. Strain, M. Sorel, J. E. Sipe, and D. Bajoni, "Micrometer-scale integrated silicon source of time-energy entangled photons," Optica **2**(2), 88–94 (2015).

31. C. Reimer, M. Kues, P. Roztocki, B. Wetzel, F. Grazioso, B. E. Little, S. T. Chu, T. Johnston, Y. Bromberg, L. Caspani, D. J. Moss, and R. Morandotti, "Generation of multiphoton entangled quantum states by means of integrated frequency combs," Science **351**(6278), 1176–1180 (2016).

32. M. Kues, C. Reimer, P. Roztocki, L. R. Cortés, S. Sciara, B. Wetzel, Y. Zhang, A. Cino, S. T. Chu, B. E. Little, D. J. Moss, L. Caspani, J. Azaña, and R. Morandotti, "On-chip generation of high-dimensional entangled quantum states and their coherent control," Nature **546**(7660), 622–626 (2017).

33. J. Wang, S. Paesani, Y. Ding, R. Santagati, P. Skrzypczyk, A. Salavrakos, J. Tura, R. Augusiak, L. Mančinska, D. Bacco, D. Bonneau, J. W. Silverstone, Q. Gong, A. Acín, K. Rottwitt, L. K. Oxenløwe, J. L. O'Brien, A. Laing, and M. G. Thompson, "Multidimensional quantum entanglement with large-scale integrated optics," Science **360**(6386), 285–291 (2018).

34. A. Rao, N. Nader, M. J. Stevens, T. Gerrits, O. S. Magaña-Loaiza, G. F. Camacho-González, J. Chiles, A. Honardoost, M. Malinowski, R. Mirin, and S. Fathpour, "Photon Pair Generation on a Silicon Chip Using Nanophotonic Periodically-Poled Lithium Niobate Waveguides," in *Conference on Lasers and Electro-Optics*, OSA Technical Digest (online) (Optical Society of America, 2018), paper JTh3C.2.

35. P. Kumar, "Quantum frequency conversion," Opt. Lett. **15**(24), 1476–1478 (1990).

36. A. Singh, Q. Li, S. Liu, Y. Yu, X. Lu, C. Schneider, S. Höfling, J. Lawall, V. Verma, R. Mirin, S. W. Nam, J. Liu, and K. Srinivasan, "Quantum frequency conversion of a quantum dot single-photon source on a nanophotonic chip," Optica **6**(5), 563–569 (2019).

37. S. Zaske, A. Lenhard, C. A. Keßler, J. Kettler, C. Hepp, C. Arend, R. Albrecht, W. M. Schulz, M. Jetter, P. Michler, and C. Becher, "Visible-to-telecom quantum frequency conversion of light from a single quantum emitter," Phys. Rev. Lett. **109**(14), 147404 (2012).

38. K. R. Parameswaran, R. K. Route, J. R. Kurz, R. V. Roussev, M. M. Fejer, and M. Fujimura, "Highly efficient second-harmonic generation in buried waveguides formed by annealed and reverse proton exchange in periodically poled lithium niobate," Opt. Lett. **27**(3), 179–181 (2002).

39. G. D. Miller, R. G. Batchko, W. M. Tulloch, M. M. Fejer, and R. L. Byer, "42%-efficient single-pass cw second-harmonic generation in periodically poled lithium niobate," Opt. Lett. **22**(24), 1834–1836 (1997).

40. S. Tanzilli, W. Tittel, H. De Riedmatten, H. Zbinden, P. Baldi, M. DeMicheli, D. Ostrowsky, and N. Gisin, "PPLN waveguide for quantum communication," Eur. Phys. J. D **18**(2), 155–160 (2002).

41. C. Langrock, E. Diamanti, R. V. Roussev, Y. Yamamoto, M. M. Fejer, and H. Takesue, "Highly efficient single-photon detection at communication wavelengths by use of upconversion in reverse-proton-exchanged periodically poled LiNbO$_3$ waveguides," Opt. Lett. **30**(13), 1725–1727 (2005).

42. S. Tanzilli, W. Tittel, M. Halder, O. Alibart, P. Baldi, N. Gisin, and H. Zbinden, "A photonic quantum information interface," Nature **437**(7055), 116–120 (2005).

43. P. Rabiei, J. Ma, S. Khan, J. Chiles, and S. Fathpour, "Heterogeneous lithium niobate photonics on silicon substrates," Opt. Express **21**(21), 25573–25581 (2013).

44. A. Rao and S. Fathpour, "Heterogeneous thin-film lithium niobate integrated photonics for electrooptics and nonlinear optics," IEEE J. Sel. Top. Quantum Electron. **24**(6), 1–12 (2018).

45. A. Rao and S. Fathpour, "Compact lithium niobate electrooptic modulators," IEEE J. Sel. Top. Quantum Electron. **24**(4), 1–14 (2018).

46. H. Liang, R. Luo, Y. He, H. Jiang, and Q. Lin, "High-quality lithium niobate photonic crystal nanocavities," Optica **4**(10), 1251–1258 (2017).

47. C. Wang, M. Zhang, R. Zhu, H. Hu, H. Chen, and M. Lončar, "On-Chip Kerr frequency comb generation in lithium niobate microresonators," in *Conference on Lasers and Electro-Optics*, OSA Technical Digest (online) (Optical Society of America, 2018), paper SW4M.3.

48. L. Chen and R. M. Reano, "Compact electric field sensors based on indirect bonding of lithium niobate to silicon microrings," Opt. Express **20**(4), 4032–4038 (2012).

49. R. Luo, H. Jiang, H. Liang, Y. Chen, and Q. Lin, "Self-referenced temperature sensing with a lithium niobate microdisk resonator," Opt. Lett. **42**(7), 1281–1284 (2017).

50. I. Krasnokutska, J.-L. J. Tambasco, X. Li, and A. Peruzzo, "Ultra-low loss photonic circuits in lithium niobate on insulator," Opt. Express **26**(2), 897–904 (2018).

51. M. A. Baghban, J. Schollhammer, C. E. Herranz, K. B. Gylfason, and K. Gallo, "Bragg gratings in thin-film LiNbO$_3$ waveguides," Opt. Express **25**(26), 32323–32332 (2017).

52. M. Prost, G. Liu, and S. J. Ben Yoo, "A compact thin-film lithium niobate platform with arrayed waveguide gratings and MMIs," in *Optical Fiber Communication Conference*, OSA Technical Digest (online) 2018, paper Tu3A.3.

53. A. Rao, A. Patil, J. Chiles, M. Malinowski, S. Novak, K. Richardson, P. Rabiei, and S. Fathpour, "Heterogeneous microring and Mach-Zehnder modulators based on lithium niobate and chalcogenide glasses on silicon," Opt. Express **23**(17), 22746–22752 (2015).

54. M. Mahmoud, S. Ghosh, and G. Piazza, "Lithium niobate on insulator (LNOI) grating couplers," in *CLEO: 2015*, OSA Technical Digest (online) 2015, paper SW4I.7.

55. Z. Chen, R. Peng, Y. Wang, H. Zhu, and H. Hu, "Grating coupler on lithium niobate thin film waveguide with a metal bottom reflector," Opt. Mater. Express **7**(11), 4010–4017 (2017).

56. A. Rao, A. Patil, P. Rabiei, A. Honardoost, R. DeSalvo, A. Paolella, and S. Fathpour, "High-performance and linear thin-film lithium niobate Mach–Zehnder modulators on silicon up to 50 GHz," Opt. Lett. **41**(24), 5700–5703 (2016).

57. S. Fathpour, "Heterogeneous nonlinear integrated photonics," IEEE J. Quantum Electron. **54**(6), 1–16 (2018).

58. F. Laurell, J. Webjorn, G. Arvidsson, and J. Holmberg, "Wet etching of proton-exchanged lithium niobate -A novel processing technique," J. Lightwave Technol. **10**(11), 1606–1609 (1992).

59. J. T. Nagy and R. M. Reano, "Periodic poling of ion-sliced X-Cut magnesium oxide doped lithium niobate thin films," in *Conference on Lasers and Electro-Optics*, OSA Technical Digest (online), 2018, paper SF2I.2.

60. J. T. Nagy and R. M. Reano, "Reducing leakage current during periodic poling of ion-sliced x-cut MgO doped lithium niobate thin films," Opt. Mater. Express **9**(7), 3146–3155 (2019).

61. P. S. Bullena, H.-C. Huangb, H. Yangb, J. I. Dadapb, I. Kymissisb, and R. M. Osgood Jr, "Microscopy and microRaman study of periodically poled domains in deeply thinned lithium niobate wafers," Opt. Mater. **57**, 243–248 (2016).

62. G. D. Miller, "Periodically poled lithium niobate: modelling, fabrication, and nonlinear-optical performance," Ph.D. thesis (Stanford University, 1998).